DTU Library

Evaluation of the capacitive behavior of 3D carbon electrodes for sub-retinal photovoltaic prosthesis

Davidsen, Rasmus Schmidt; Hemanth, Suhith; Keller, Stephan Sylvest; Bek, Toke; Hansen, Ole

Link back to DTU Orbit

Research paper

Evaluation of the capacitive behavior of 3D carbon electrodes for sub-retinal photovoltaic prosthesis

Rasmus Schmidt Davidsen[a,*], Suhith Hemanth[a], Stephan Sylvest Keller[a], Toke Bek[b], Ole Hansen[a]

[a] Department of Micro- and Nanotechnology, Technical University of Denmark (DTU), Denmark
[b] Department of Ophthalmology, Aarhus University Hospital, Denmark

ABSTRACT

Here, we evaluate if microfabricated 3D pyrolytic carbon electrodes are suitable for application in sub-retinal photovoltaic prosthesis. This is done by measuring the charge storage capacity (CSC) and the maximum injectable charge, which indicate if the electrodes allow accumulation of sufficiently high charges in the charge cycle and are able to provide sufficiently fast discharge to stimulate neurons, respectively. The CSC was determined to 10.9 mC/cm^2 for carbon pillars and 6.4 mC/cm^2 for planar carbon electrodes. These values are comparable with values obtained for state-of-the-art electrode materials applied for retinal stimulation such as iridium oxide (IrO$_x$). The maximum injectable charge was determined from cyclic voltammograms (CV) with values of 1.0 and 1.7 mC/cm^2 for planar and pillar carbon electrodes, respectively. The measured contact resistance between carbon and n + doped Si confirms that pyrolytic carbon is a possible candidate for integration as a 3D electrode material on photovoltaic silicon retinal implants. The elemental composition of the fabricated pyrolytic carbon pillars was analyzed by X-ray photoelectron spectroscopy (XPS). The analysis showed that the Al$_2$O$_3$ passivated sample with fabricated pyrolytic carbon pillars only contained aluminum, oxygen and carbon, indicating a successful pyrolysis process without any unwanted elements. The study shows promising potential for pyrolytic carbon as a material for 3D electrodes in retinal, photovoltaic implants.

1. Introduction

Retinal diseases are the most frequent causes of visual loss in the Western world. Two of the prominent diseases are age-related macular degeneration (AMD) diagnosed in 700,000 individuals annually alone in the US, and retinitis pigmentosa (RP) which is diagnosed for 1 out of 4000 live births [1]. The detailed pathophysiology of AMD and RP is unknown, but a central event leading to visual loss in these diseases is the degeneration of retinal photoreceptors. At present, there are no effective treatments of photoreceptor degeneration. A promising potential solution for partial restoration of sight is to implant a solar (photovoltaic) cell array that can translate the incoming light into an electrical signal to be transmitted to the secondary neurons in the retina [2–5].

A solar cell is a photodiode, which produces an electrical output directly from incoming light in the relevant wavelength range. By placing an array of electrically separated photodiodes or solar cells at the location of lost photoreceptors and in contact with the overlying retina, stimulation of the secondary neurons will occur when light is incident on the eye. The restoration of vision using photodiodes is limited by 1) the resolution (pixel density) of the solar cell array, 2) the sensitivity of the solar cells to the incident light and 3) the connection of the solar cell to the secondary neurons in the retina.

Palanker et al. [6,7] demonstrated the fabrication of a photovoltaic array with pixel sizes down to $70 \times 70\,\mu m^2$ and a responsivity of 0.36 A/W. Zrenner et al. [8] demonstrated a similar array with 1500 photodiodes, and the study confirmed a satisfactory object recognition and overall meaningful detailed vision in previously blind patients. However, it remains a major challenge to obtain a sufficiently high light sensitivity and optimal connection of an implantable photovoltaic array to the secondary retinal neurons [6–8]. The latter may be improved by creating 3D structures [9] that enhance the migration of retinal tissue and cells into voids and cavities at the tissue-implant interface. It has been reported [10] that pillars with 10 μm diameter, 40 μm height and 40 μm center-to-center spacing lead to significant migration of both Müller cells and inner nuclear layer cells. Such structures were typically defined in the photosensitive polymer SU-8, but no electrically active 3D electrodes for retinal implants have been reported to date.

In order to improve contact between stimulating electrodes in sub-retinal photovoltaic implants and the surrounding tissue, electrically

---

active 3D interfaces might be realized. Enhanced charge transfer between 3D stimulating electrodes and the neural tissue might enable a smaller minimum 'pixel' area and thereby higher resolution in the prosthetic vision, which is the final goal. This study focuses on fabrication of 3D carbon electrodes and evaluation of their properties with the perspective of potential integration in sub-retinal photovoltaic implants. 3D carbon electrodes were obtained by pyrolysis of the negative photoresist SU-8 at temperatures of $900 °C$ in inert atmosphere. SU-8 is very suitable for fabricating high aspect ratio microstructures with dimensions relevant for sub-retinal neural stimulation [11]. Pyrolyzed SU-8 has been reported to be conductive with sheet resistance below 100Ω [12,13], biocompatible and promote adhesion and differentiation of human neuronal stem cells [14]. Thus, 3D pyrolytic carbon electrodes made from SU-8 seem promising for application in a sub-retinal prosthesis. However, the electrical properties of carbon pillar electrodes on silicon must be investigated. More specifically, i) the contact resistance between carbon and doped Si must be sufficiently small to minimize resistive losses, ii) the charge storage capacity (CSC) must be high to allow accumulation of sufficiently high charges in the photovoltaic charge cycle and iii) the injectable charge must be large to provide sufficiently fast discharge to stimulate neurons. Furthermore, the pyrolytic carbon electrodes should not contain any residues of toxic elements.

2. Materials and methods

2.1. Measurement of contact resistance

For characterization of the contact resistance between carbon and Si Kelvin resistor contact resistance patterns were fabricated. First, highly n-doped regions were defined in a p-type double-side polished Czochralski (CZ) silicon wafer (4″ diameter, $350 \mu m$ thick, 0.4Ω-cm) using phosphorus diffusion at $900 °C$ for 30 min with $POCl_3$ as dopant source in a Tempress tube furnace with a 500 nm thermal SiO_2 patterned by photolithography as a mask. Contact windows were etched in the SiO_2 mask by buffered HF. The SiO_2 was kept on the device as an insulation layer on the front. Finally, pyrolytic carbon pads were fabricated with a method similar to the one described earlier [15]. Briefly, SU-82075 (Microchem, USA) was spun to a thickness of $78 \mu m$ using a Süss MicroTec-RCD8T spin coater with a spin speed of 2000 rpm for 60 s after an initial spreading at 700 rpm for 30 s. The polymer was softbaked on a hot plate at $50 °C$ for 5 h, exposed to a dose of 210 mJ/cm^2 UV radiation and post exposure baked at $50 °C$ for 5 h. The structures were developed in PGMEA for 2×10 min, treated with a 500 mJ/cm^2 UV 'flood-exposure' and a second hard bake at $90 °C$ for 15 h. The SU-8 structures were then pyrolyzed in an ATV-PEO604 furnace at $900 °C$ for 1 h following a preheat treatment at $200 °C$ for 30 min. This process resulted in a carbon layer with a thickness of approximately $40 \mu m$ measured by a Dektak stylus profiler. The test structures consisted of square contact windows with two different side-lengths (15 and $50 \mu m$), in which direct contact was made between n-doped Si and pyrolytic carbon. The size of the contact windows was chosen to be comparable to the intended electrode size in the final device. The remaining surface was isolated by SiO_2. Electrical contact to all four external probes was made via large (1 mm diameter) circular pyrolytic carbon pads. The design and symmetry of the Kelvin resistor test structures ensure that, in principle, only the contact resistance at the contact window in the center of the structure is extracted.

The contact resistance between n^+ Si and pyrolytic carbon electrodes was measured on the 'Kelvin resistor' test structures seen in Fig. 1 by applying a current through two opposing terminals and recording the voltage difference across the remaining two terminals. In the ideal Kelvin measurement structure a current is injected and extracted using two electrodes on two different conducting layers while the potential difference across the contact between the layers is measured between two current-less electrodes on the same two layers. In

real structures, with potential linewidth and alignment errors, the measured resistance is larger due to the so-called spreading resistance R_g. However, the magnitude of R_g can be minimized by proper design of the structure. Plotting voltage as a function of current is expected to yield a linear relationship with a slope equal to the Kelvin resistance, R_K, defined as [16]:

$$R_K = \frac{\rho_c}{A_c} + R_g,$$

where ρ_c is the specific contact resistance, A_c is the contact area and R_g is a parasitic, geometry-dependent resistance term, which can be neglected if the arm width is equal to the hole width in the design of the Kelvin resistor, such as shown in Fig. 1. Two dimensional numerical simulations of current spreading have shown that the geometrical term, R_g, can be significantly reduced using a so-called D-type resistor, where the arm width equals the contact hole width [17].

For the determination of the charge injection properties, electrode chips with $4 mm^2$ working electrodes (WE) with pyrolytic carbon pillars were used. The design and fabrication of these test structures is described elsewhere [15]. The CSC was characterized using cyclic voltammetry (CV) with 10 mM potassium hexa-cyano ferrate (II + III) in phosphate buffered saline (PBS, pH = 7) as the electrolyte. CV and transient voltammograms were measured using a CHI 1030 potentiostat and NOVA software for data collection. The scan rate was 100 mV/s in all experiments.

The charge storage capacity (CSC) was extracted from measured cyclic voltammograms, as the integration of the cathodic (CSC_{cat}) or anodic (CSC_{an}) part of the curve divided by the electrode surface area A_e (cm^2) and sweep rate s (V/s), according to.

$$CSC_{cat} = \frac{\int_{V_{min}}^{0} I(V)dV}{A_e \cdot s},$$

$$CSC_{an} = \frac{\int_{0}^{V_{max}} I(V)dV}{A_e \cdot s},$$

where I is the current, V is the voltage.

The maximum injectable charge Q_{max} for pillars and planar pyrolytic carbon electrodes, respectively, was calculated from the extracted threshold-time t_{th} and the constant current I, i.e. $Q_{max} = I t_{th}/A_e$ where A_e is the electrode area, was determined using transient voltage measurements. In order to determine Q_{max} for short current pulses, a constant current I was applied and the resulting voltage was measured as function of time. The threshold-time t_{th} at which the voltage reached a predefined threshold value V_{th} was then multiplied with the constant current in order to calculate the charge. The voltage threshold V_{th} was defined as the local minimum on the CV curve.

The elemental composition of the sample was characterized using X-ray photoelectron spectroscopy (XPS). The measurement and analysis was carried out using a Thermo Scientific K-alpha XPS tool with a monochromatic aluminum K-α source. Binding energy surveys in the range 0 to 1350 eV were performed. The software package, Avantage, was used for the analysis of the spectra. In order to study the elemental depth profile, 10 sequential XPS surveys where made; each after an etch time of 10 s (10 keV).

3. Results and discussion

3.1. Contact resistance

Fig. 1 shows optical microscope images of the fabricated Kelvin resistor structures before and after deposition of SU-8. Measurements were performed on pyrolyzed SU-8. The side length of the contact window in the center was 15 and $50 \mu m$, respectively, the arm width
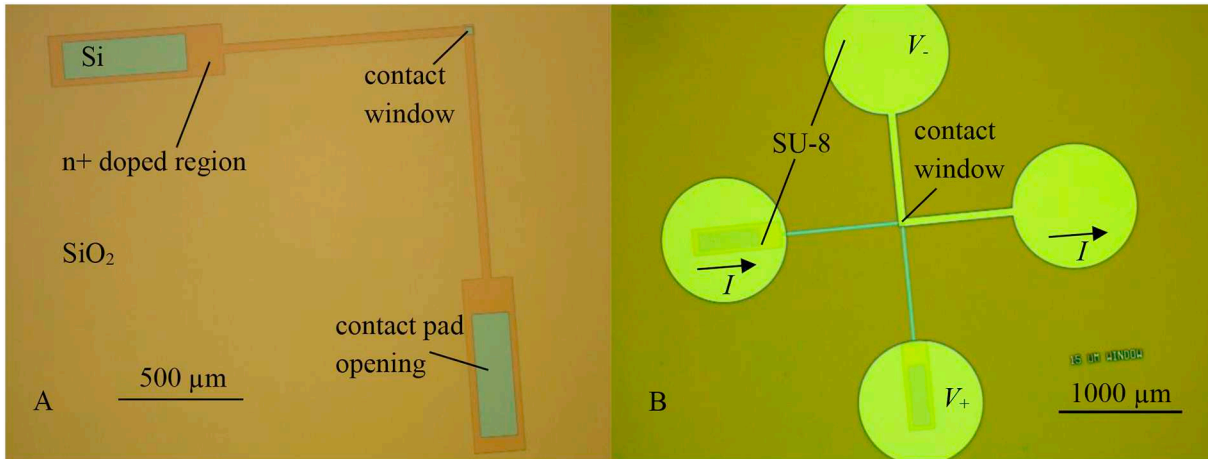
Fig. 1. 'Kelvin resistor' structures with n$^+$ Si and SiO$_2$ mask without (A) and with (B) SU-8 pads used for contact resistance measurements. *I* indicates current injection and extraction (as indicated by arrows) while V_- and V_+ indicate voltage sensing at two sets of opposing electrodes.

was kept equal to the contact window side length and contact pads were made sufficiently large (Ø1 mm) such that the size of the pads should not affect the resistance measurement.

Fig. 2 shows the measured voltage at different currents in the range of 0–20 μA. The current range was chosen in order to measure in a voltage range significantly lower than the expected operating voltage of ~ 0.6 V for a single-diode silicon photovoltaic device. The linear regressions yield Kelvin resistances of 5.6 kΩ and 8.4 kΩ for 50 μm and 15 μm wide contact windows, respectively. We note that the magnitude of the Kelvin resistance for the 15 and 50 μm contact windows, respectively, differ from the expected inverse proportionality with area ($R_K = \rho_c/A_c$). We explain this deviation with 1) partial delamination of the carbon, which was observed on larger carbon-coated areas; 2) effects of mask mis-alignment such that the real geometry differs from the ideal Kelvin geometry and R_g becomes important. By multiplying the Kelvin resistance with the contact window area this results in specific contact resistances of 140 mΩ cm^2 and 19 mΩ cm^2, respectively. For the 3D carbon electrodes in the final photovoltaic implant the desired diameter of the pillar electrodes is 15 μm. For these structures the calculated contact resistance is 11 kΩ, using the value for the 15 μm wide contact window, which is more comparable to the actual electrode geometry in terms of size, and which is less susceptible to measurement error than the larger contact. In a sub-retinal implant it is essential that charge is injected from the electrodes to the neural tissue. Such charge injection has to overcome the spreading resistance

$$R_{sp} = \frac{\rho}{2\pi r} = \frac{1.67\ \Omega m}{2\pi \times 7.5 \times 10^{-6} m} = 35\ k\Omega,$$

where ρ is the resistivity of the surrounding medium [18,19] and *r* is the radius of a hemispherical contact, in this case 7.5 μm.

A successful electrode in a subretinal implant should not have a contact resistance significantly higher than the spreading resistance. Thus, since the measured contact resistance is smaller than the spreading resistance, the result confirms that pyrolytic SU-8 might indeed be used as an electrode material directly on highly doped Si.

3.2. Charge injection properties

In order for a material to be appropriate as an electrode in a sub-retinal implant, it must be able to handle sufficiently large charge without electrolysis of the electrode itself or the surrounding medium. Fig. 3 shows cyclic voltammograms recorded with a planar pyrolytic carbon electrode and different designs of pyrolytic carbon pillar electrodes.

The values of CSC were extracted for different chip designs, including different size and pitch of pyrolytic carbon pillars (Table 1). Fig. 4 shows CSC plotted as function of effective area (normalized to projected plane area; for a planar electrode $A_{eff} = 1$). All electrodes had a circular projected area of 0.126 cm^2.

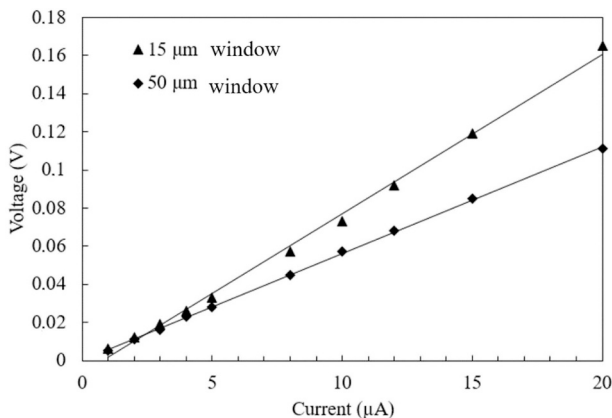Fig. 4 shows that CSC scales linearly with effective area, which

Fig. 2. Voltage-current measurement on test structures with pyrolyzed SU-8 contacts on n$^+$ Si. The linear fit-lines yield slopes of 0.0084 and 0.0056 V/μA (Kelvin resistances of 8.4 and 5.6 kΩ) for the 15 and 50 μm contact windows, respectively.
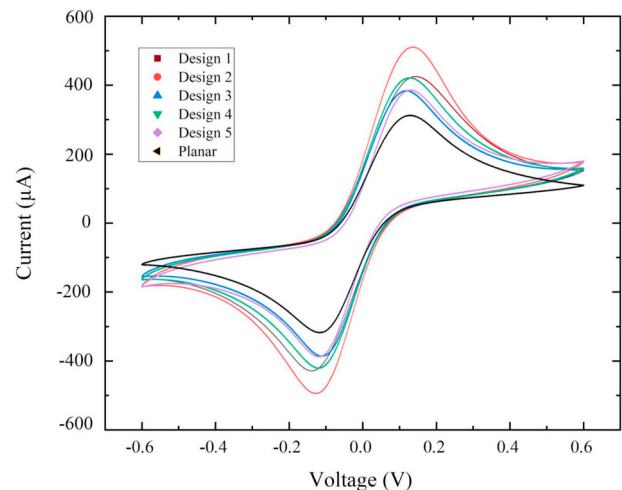

Fig. 3. Cyclic voltammogram (CV) measured with pyrolytic carbon planar and pillar electrodes. Details of the five different pillar designs are shown in Table 1.

Table 1

Dimensions of the different pyrolytic carbon pillar designs including pillar diameter, height, pitch between pillars, effective area and measured charge storage capacity.

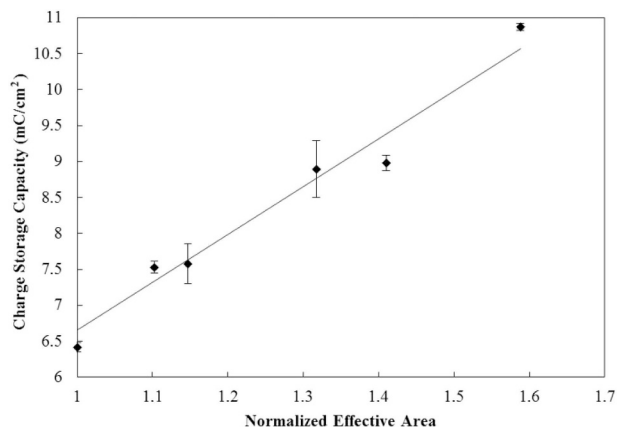| Post-pyrolysis	Pillar Diameter (µm)	Pitch (µm)	Pillar Height (µm)	A_{eff}	CSC (mC/cm^2)
Design 1	6.7	50	36	1.3	8.9
Design 2	12	50	36	1.6	10.9
Design 3	12	100	36	1.2	7.6
Design 4	30	100	36	1.4	9.0
Design 5	30	200	36	1.1	7.5
Planar	–	–	–	1.0	6.4

Fig. 4. Values of charge storage capacity (CSC) extracted from CV-curves for different carbon pillar geometries, plotted as function of normalized effective surface area, A_{eff}, where $A_{eff} = 1$ is a planar carbon electrode. The slope of the linear fit line is 6.65 mC/cm^2.

indicates rather homogenous pyrolytic carbon structures. The linear trend-line in Fig. 4 was forced through (0,0).

Fig. 5 shows measured voltage as function of time at constant current of 1 mA. It should be noted that the initial voltage step, V_R, is ohmic and is due to series resistance. This voltage step must be corrected for to arrive at the actual voltage threshold defined as V_{th}. Thus, the threshold-time, t_{th}, was extracted at $V = V_{th} + V_R$. Table 2 shows extracted threshold-times and the maximum injectable charge calculated for planar and pillar electrodes (Design 2).

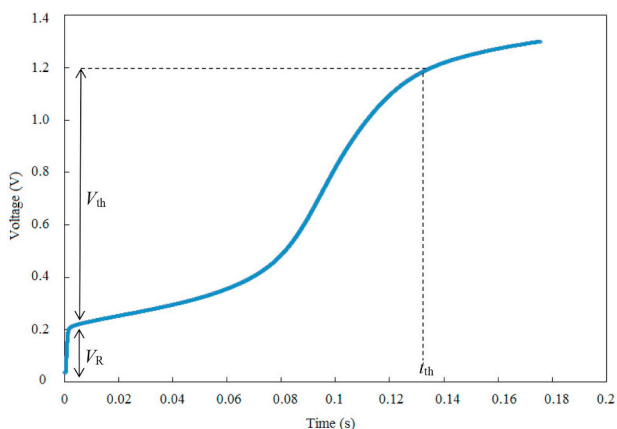**Fig. 5.** Transient voltage measurements at a constant current of 1 mA for a planar pyrolytic carbon electrode. The initial voltage step V_R is ohmic and due to series resistance. The threshold voltage V_{th} must be corrected for the ohmic voltage drop when the threshold-time t_{th} and thus the maximum injectable charge are calculated.

Table 2

Extracted threshold-time corresponding to the threshold voltage at constant current of 1 mA from transient voltage curves.

	Threshold-time t_{th} (s)	Current I (mA)	Injectable Charge Q_{max} (mC/cm^2)
Pillars	0.212	1.0	1.69
Planar	0.130	1.0	1.03

3.3. XPS analysis

Fig. 6 shows a stacked chart of the recorded XPS spectra, where the bottom spectrum is the first measurement obtained at the top surface of the sample.

The measured XPS spectra were analyzed in order to identify the relevant peaks that represent elements present in the sample. The three most important peaks are easily identified: Oxygen (O1s) at 532.43 eV, carbon (C1s) at 285.16 eV and aluminum (Al2p) at 75.97 eV. The presence of these elements agrees well with the sample processing, since pyrolytic carbon pillars were fabricated on a Si wafer passivated with Al_2O_3. The peak at 121 eV is attributed to Al2s. The identified peak assignments are indicated in Fig. 6. At higher binding energies the Auger lines from the KVV-series of C (1220 eV) and O (980 and 1010 eV) are identified, respectively. KVV refers to the KLL Auger series, where the vacancies in the L-shell are in the valence level [20,21]. The small peak around 40 eV is attributed to implanted Ar, which arises from the Ar ions used for sputter etching in the depth profiling. This explains why the peak at 240 eV is not present in the level 0 spectrum, which was taken before the depth profiling.

Table 3 shows the peak data and the calculated elemental fractions of the three important, elemental peaks for the level 0 and level 10 measurements shown in Fig. 6.

Based on the 10 different spectra, measured at increasing depths from the top of the sample, the elemental constitution (atomic %) as function of etch time can be plotted. Fig. 7 shows the calculated elemental fractions of carbon, oxygen, aluminum and argon as function of the etch time, which represents the etch depth.

The result shows that the Al and O content increases while the C content decreases with etch time. A detailed interpretation of the elemental fractions is quite difficult since a heterogeneous surface of pyrolytic carbon pillars on an Al_2O_3 surface is probed. The projected fractional area covered by carbon pillars is approximately 20% assuming 20 µm wide, cylindrical pillars with a pitch of 40 µm. The atomic density in the pyrolytic carbon is however much higher than that of Al_2O_3, and therefore the C related signal strength is expected to be larger than what might be expected by just comparing the fractional areas. Furthermore, this observation may partially be explained by C-related contamination on the bare Al_2O_3 surface, which additionally increases the carbon signal measured on the surface and reduces Al and O related signals; as the contamination erodes away the C signal reduces while Al and O signals increase. We note that in the level 10 XPS scan, the ratio of atomic fractions of O and Al is the one of stoichiometric Al_2O_3, i.e., an experimental ratio of 1.56 versus the exact stoichiometric ratio of 1.5. Importantly, it has to be noted that there are no
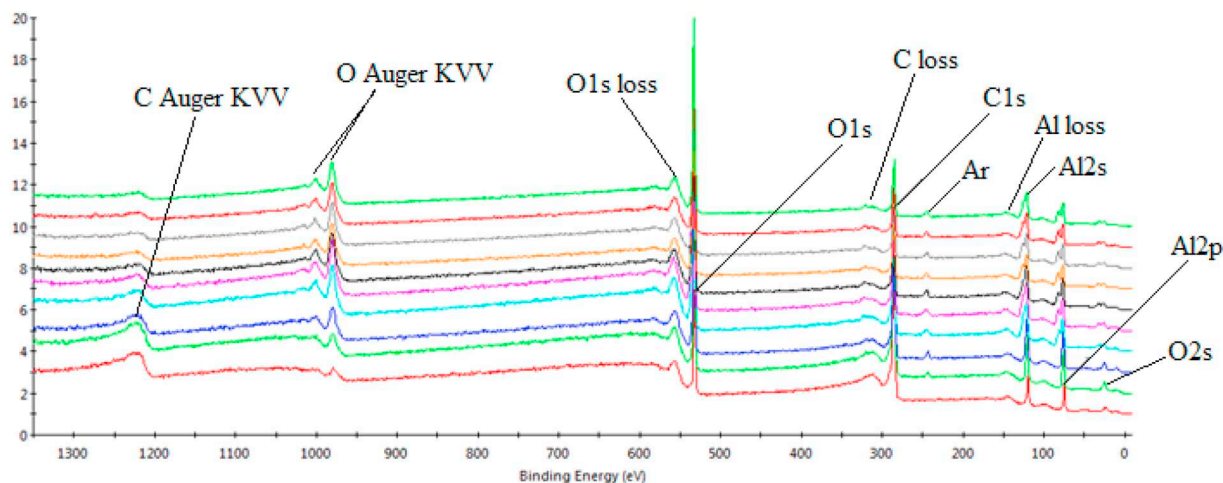
Fig. 6. Ten different XPS spectra obtained from the same sample with pyrolytic carbon pillars on an Al_2O_3-passivated Si wafer, at different etch depths. The lowermost spectrum is from the original surface; the remaining spectra are obtained after sequential sputter etching for 10 s.

Table 3
Peak data extracted from the XPS spectrum shown in Fig. 6. The elemental composition is calculated based on the area under each peak.

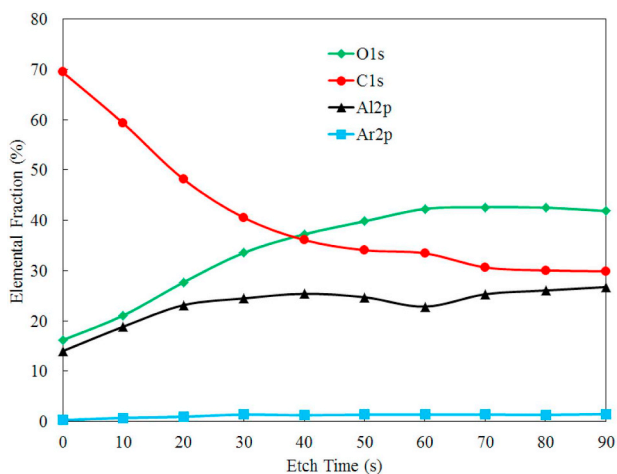| Name	Peak position (eV)	FWHM (eV)	Peak area (keV/s)	Fraction (atomic %)	Fraction (atomic %)
		Level 0	Level 0	Level 0	Level 10
Al2p	74.97	2.75	57.7	14.0	26.8
C1s	285.05	2.77	450.8	69.5	29.9
Ar2p	239.64	1.75	7.2	0.5	1.5
O1s	531.88	3.10	254.1	16.0	41.8

Fig. 7. Calculated elemental fractions of carbon, oxygen and aluminum as function of the etch time, which represents the depth from the top of the sample (etch time 0 s).

un-expected peaks in the XPS spectra, which indicates that the pyrolytic carbon pillars do not contain toxic elements in significant quantities.

3.4. Pyrolytic carbon pillar electrode fabrication

Fig. 8 shows optical microscope images of the final design of pyrolytic carbon pillars after lithography. The successfully developed pillars have the intended geometry with a center-to-center pitch at the bottom of 40 μm and a pillar width of 17–20 μm at the bottom and ~11 μm wide at the top. Fig. 8 shows that pillars are slightly wider at the base, which may be an advantage for electrical contact and

mechanical stability. However, in a few cases delamination of pillars after development was observed (Fig. 8, right).

Fig. 9 shows SEM-images of the pyrolytic carbon pillars obtained from SU-8. The pillars are approximately 35 μm in height, 11 μm in diameter at the top and placed with a center-to-center pitch of 40 μm. The SEM images confirm the observations that the width is slightly larger at the base of the pillars compared to the top.

4. Conclusions

Pyrolytic carbon pillars with appropriate dimensions for sub-retinal implant electrodes were fabricated and characterized. The measured contact resistance confirms that pyrolytic carbon is a possible candidate as a 3D electrode material on photovoltaic silicon retinal implants. The contact resistance between pyrolytic carbon and n + doped Si is smaller than the spreading resistance in surrounding tissue from hemispherical electrodes with the same radius as the pillars. This indicates that pyrolytic carbon may be able to efficiently conduct current from local pn-junctions in the Si device. The contact resistance may be reduced further if metal silicide (e.g. $TiSi_2$) contacts on n + Si are included in the process. The charge storage capacity was determined to 10.9 mC/cm^2 for the best 3D carbon pillar geometries and 6.4 mC/cm^2 for planar carbon electrodes. Such values are comparable with those of IrO_x electrodes [22,23], which are considered the state-of-the-art and material of choice for retinal stimulation. The maximum injectable charge of similar carbon electrodes determined from transient voltage measurements was in the range 1–1.7 mC/cm^2 for planar and pillar carbon electrodes. These values are encouraging for future application of pyrolytic carbon electrodes in sub-retinal implants, since retinal stimulation is possible for much lower charge densities [22,24], while significantly higher charge densities are irrelevant due to tissue damage thresholds [24,25]. It is noteworthy that pillar electrodes yield higher CSC and injectable charge compared to planar references. This suggests that even higher charge densities might be realized in future studies by
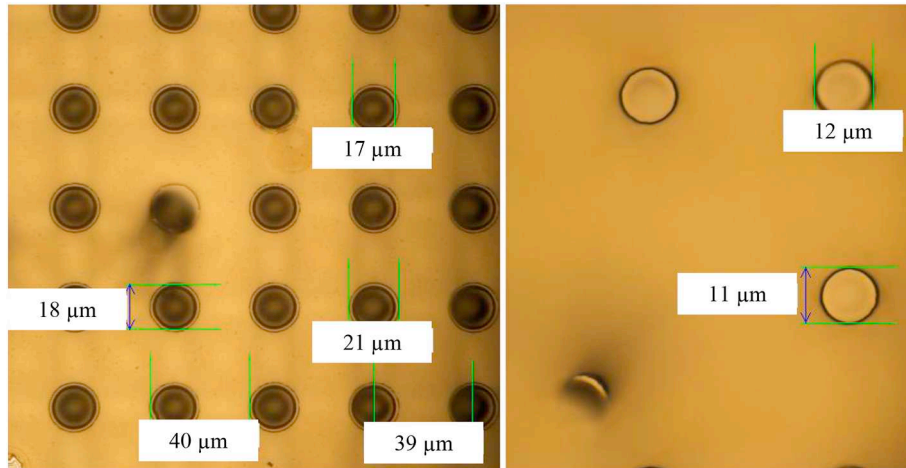
Fig. 8. Optical microscope image of pyrolytic carbon pillars with dimensions measured at the bottom (A) and top (B) of the pillars. Center-to-center pitch at the bottom is 40 μm and pillar width is 17–20 μm at the bottom, while pillars seem to be ∼ 11 μm wide at the top.

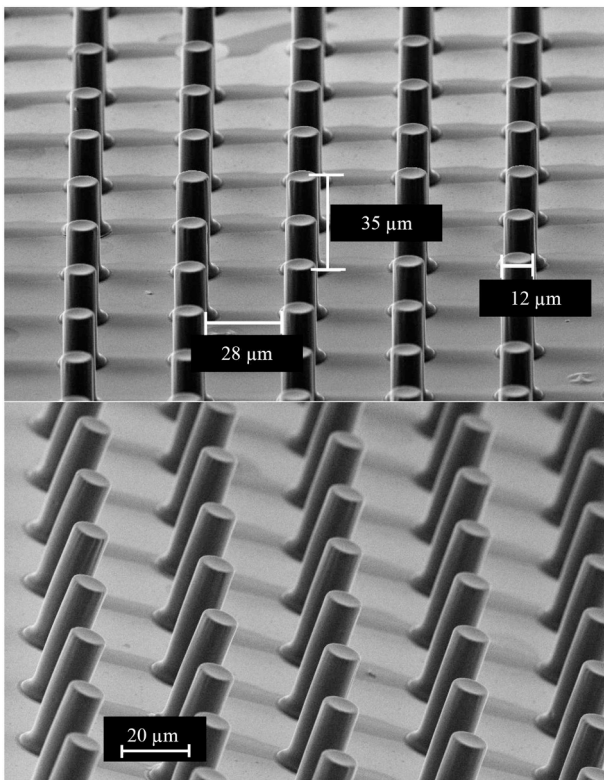**Fig. 9.** Scanning electron microscope (SEM) images of pyrolytic carbon pillars made from SU-8. Pillars are ∼35 μm in height, ∼12 μm in diameter and placed with a center-to-center pitch of ∼40 μm.

further optimizing the pillar geometry and fabrication. The elemental composition of the fabricated pyrolytic carbon pillars was analyzed by XPS. The analysis showed that the pyrolysis was successful and clean. We expect in future work to significantly improve the electrical properties of the pyrolytic carbon electrodes.

In conclusion, the combined measurements with 3D pyrolytic carbon electrodes show promising potential within the target application for photovoltaic sub-retinal implants, since sufficient charge injection is realistic, ideal dimensions may be realized in practice, 3D electrodes may be fabricated on a perforated photovoltaic Si chip without critical fabrication constraints and the material seems to be pure carbon without trace elements that could jeopardize biocompatibility.

At present the fabrication of complete implants, ready for in vitro tissue measurements, is ongoing.

Acknowledgements

References

[1] J.D. Loudin, D.M. Simanovkskii, K. Vijayraghavan, C.K. Sramek, A.F. Butterwick, P. Huie, G.Y. McLean, D.V. Palanker, Optoelectronic retinal prosthesis: system design and performance, J. Neural Eng. 4 (2007) 72–84, https://doi.org/10.1088/1741-2560/4/1/S09.

[2] Y. Mandel, G. Goetz, D. Lavinsky, P. Huie, K. Mathieson, L. Wang, T. Kamins, L. Galambos, R. Manivanh, J. Harris, D. Palanker, Cortical responses elicited by photovoltaic subretinal prostheses exhibit similarities to visually evoked potentials, Nat. Commun. 4 (2013) 1980, https://doi.org/10.1038/ncomms2980.

[3] S.Y. Kim, S. Sadda, J. Pearlman, M.S. Humayun, E. de Juan Jr., B.M. Melia, W.R. Green, Morphometric analysis of the macula in eyes with disciform age-related macular degeneration, Retina 22 (2002) 471–477, https://doi.org/10.1097/00006982-200208000-00012.

[4] F. Mazzoni, E. Novelli, E. Strettoi, Retinal ganglion cells survive and maintain normal dendritic morphology in a mouse model of inherited photoreceptor degeneration, J. Neurosci. 28 (2008) 14282–14292, https://doi.org/10.1523/JNEUROSCI.4968-08.2008.

[5] J.L. Stone, W.E. Barlow, M.S. Humayun, E. de Juan Jr., A.H. Milam, Morphometric analysis of macular photoreceptors and ganglion cells in retinas with retinitis pigmentosa, Arch. Ophthalmol. 110 (1992) 1634–1639, https://doi.org/10.1001/archopht.1992.01080230134038.

[6] L. Wang, K. Mathieson, T.I. Kamins, J.D. Loudin, L. Galambos, G. Goetz, J.S. Harris, D.V. Palanker, Photovoltaic retinal prosthesis: implant fabrication and performance, J. Neural Eng. 9 (2012) 046014, , https://doi.org/10.1088/1741-2560/9/4/046014.

[7] K. Mathieson, J. Loudin, G. Goetz, P. Huie, L. Wang, T.I. Kamins, L. Galambos, R. Smith, J.S. Harris, A. Sher, D. Palanker, Photovoltaic retinal prosthesis with high pixel density, Nat. Photonics 6 (2012) 391–397, https://doi.org/10.1038/nphoton.2012.104.

[8] E. Zrenner, K.U. Bartz-Schmidt, H. Benav, D. Besch, A. Bruckmann, V.P. Gabel, F. Gekeler, U. Greppmaier, A. Harscher, S. Kibbel, J. Koch, A. Kusnyerik, T. Peters, K. Stingl, H. Sachs, A. Stett, P. Szurman, B. Wilhelm, R. Wilke, Subretinal electronic chips allow blind patients to read letters and combine them to words, Proc. R. Soc. Lond. B Biol. Sci. 278 (2011) 1489–1497, https://doi.org/10.1098/rspb.2010.1747.

[9] D. Palanker, A. Vankov, P. Huie, S. Baccus, Design of a high-resolution optoelectronic retinal prosthesis, J. Neural Eng. 2 (1) (2005) S105, , https://doi.org/10.1088/1741-2560/2/1/012.

[10] G.A. Goetz, D.V. Palanker, Electronic approaches to restoration of sight, Rep. Prog. Phys. 79 (2016) 096701, , https://doi.org/10.1088/0034-4885/79/9/096701.

[11] L. Amato, S.S. Keller, A. Heiskanen, M. Dimaki, J. Emnéus, A. Boisen, M. Tenje, Fabrication of high-aspect ratio SU-8 micropillar arrays, Microelectron. Eng. 98 (2012) 483–487, https://doi.org/10.1016/j.mee.2012.07.092.

[12] L. Amato, A. Heiskanen, R. Hansen, L. Gammelgaard, T. Rindzevicius, M. Tenje, J. Emnéus, S.S. Keller, Dense high-aspect ratio 3D carbon pillars on interdigitated microelectrode arrays, Carbon 94 (2015) 792–803, https://doi.org/10.1016/j.

carbon.2015.06.014.

[13] Y.M. Hassan, C. Caviglia, S. Hemanth, D.M.A. Mackenzie, T.S. Alstrøm, D.H. Petersen, S.S. Keller, High temperature SU-8 pyrolysis for fabrication of carbon electrodes, J. Anal. Appl. Pyrolysis 125 (2017) 91–99, https://doi.org/10.1016/j.jaap.2017.04.015.

[14] L. Amato, A. Heiskanen, C. Caviglia, F. Shah, K. Zór, M. Skolimowski, M. Madou, L. Gammelgaard, R. Hansen, E.G. Seiz, M. Ramos, T.R. Moreno, A. Martinez-Serrano, S.S. Keller, J. Emnéus, Pyrolysed 3D-carbon scaffolds induce spontaneous differentiation of human neural stem cells and facilitate real-time dopamine detection, Adv. Funct. Mater. 24 (44) (2014) 7042–7052, https://doi.org/10.1002/adfm.201400812.

[15] S. Hemanth, C. Caviglia, S.S. Keller, Suspended 3D pyrolytic carbon microelectrodes for electrochemistry, Carbon 121 (2017) 226–234, https://doi.org/10.1016/j.carbon.2017.05.090.

[16] D.K. Schroder, Semiconductor Material and Device Characterization, John Wiley & Sons, 2006.

[17] R.L. Gillenwater, M.J. Hafich, G.Y. Robinson, The effect of lateral current spreading on the specific contact resistivity in D-resistor kelvin devices, IEEE Trans. Electron Devices 34 (3) (1987) 537–560, https://doi.org/10.1109/T-ED.1987.22960.

[18] C. Gabriel, A. Peyman, E.H. Grant, Electrical conductivity of tissue at frequencies below 1 MHz, Phys. Med. Biol. 54 (2009) 4863–4878, https://doi.org/10.1088/0031-9155/54/16/002.

[19] K. Loizos, A.K. RamRakhyani, J. Anderson, R. Marc, G. Lazzi, On the computation of a retina resistivity profile for applications in multi-scale modeling of electrical stimulation and absorption, Phys. Med. Biol. 61 (12) (2016) 4491–4505, https://doi.org/10.1088/0031-9155/61/12/4491.

[20] D. Briggs, "Surface Analysis of Polymers by XPS and Static SIMS", Book, Cambridge University Press, 1998.

[21] B. Singh, M. Camps-Arbestain, J. Lehmann, Biochar: A Guide to Analytical Methods, CSIRO Publishing, 2017.

[22] J.D. Weiland, W. Liu, M.S. Humayun, Retinal prosthesis, Annu. Rev. Biomed. Eng. 7 (2005) 361–401, https://doi.org/10.1146/annurev.bioeng.7.060804.100435.

[23] J.D. Weiland, D.J. Anderson, M.S. Humayun, In vitro electrical properties for iridium oxide versus titanium nitride stimulating electrodes, IEEE Trans. Biomed. Eng. 49 (12) (2002) 1574–1579, https://doi.org/10.1109/TBME.2002.805487.

[24] J.F. Rizzo, J. Wyatt, J. Loewenstein, S. Kelly, D. Shire, Methods and perceptual thresholds for short-term electrical stimulation of human retina with microelectrode arrays, Invest. Ophthalmol. Vis. Sci. 44 (12) (2003) 5355–5361, https://doi.org/10.1167/iovs.02-0819.

[25] S.F. Cogan, K.A. Ludwig, C.G. Welle, P. Takmakov, Tissue damage thresholds during therapeutic electrical stimulation, J. Neural Eng. 13 (2) (2016) 021001, , https://doi.org/10.1088/1741-2560/13/2/021001.